
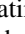

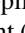



## Role of local atomic short-range order distribution in alloys: Why it matters in Si-Ge-Sn alloys

Xiaochen Jin , Shunda Chen , Christopher Lemkan , and Tianshu Li \*

Department of Civil and Environmental Engineering, George Washington University, Washington, DC 20052, USA

 (Received 18 September 2023; accepted 23 October 2023; published 13 November 2023)

Short-range order (SRO) in alloys refers to deviations from a perfectly random distribution of atoms in lattice sites within a short distance. Conventionally, the degree of the deviations has been quantified using an average SRO parameter, but such a coarse-grained description does not reflect how the deviations occur at a finer level. Here we show the distribution of the local atomic SRO parameter, which describes the occurring frequency of a local structural motif, carries the crucial information for both structures and properties in Si-Ge-Sn alloy system. This is demonstrated through the fact that distinct SRO structures can exhibit the same average SRO parameter but very different distributions and disparate electronic structures. By deliberately creating special structures that explicitly match the structural information at different levels, we show the distribution of local atomic SRO parameters contain critical structural features that are missing in the average SRO parameter but can substantially contribute to material's properties. Our finding thus calls for the need for considering the finer structural details to effectively describe alloys' structures and properties.

DOI: [10.1103/PhysRevMaterials.7.L111601](https://doi.org/10.1103/PhysRevMaterials.7.L111601)

Short-range order (SRO), featured by an atomic distribution deviating from a random solid solution within a short distance, has been demonstrated to play a decisive role in impacting various material properties over a wide range of alloy systems [1–16]. The degree of SRO can be quantified by the Warren-Cowley SRO parameter [17], which is defined as

$$\overline{\alpha}_{ij}^m = 1 - \frac{\overline{p}_{ij}^m}{c_j}, \quad (1)$$

where  $c_j$  is the concentration of species  $j$ , and  $\overline{p}_{ij}^m$  is the probability of finding atomic species  $j$  in the  $m$ th coordination shell surrounding the atomic species  $i$ . The SRO parameter can be applied as a bulk parameter to describe the overall enhancement ( $\overline{\alpha}_{ij}^m < 0$ ) or depletion ( $0 < \overline{\alpha}_{ij}^m < 1$ ) of pair  $ij$  at a specific shell  $m$  with respect to a random atomic distribution, determined by averaging the number of atomic species  $j$  surrounding each atomic species  $i$ . This can be directly measured by diffraction experiments through the Fourier transformation between real-space radial distribution function and  $k$ -space structural factor. Indeed, the SRO parameter has been commonly employed in such a way to quantify the overall degree of SRO of alloys [9–13, 15, 16, 18].

However, it remains as a question of whether such a “mean-field” parameter  $\overline{\alpha}_{ij}^m$  can sufficiently describe the structural signature of alloys. Indeed, it has been earlier recognized that such an average SRO parameter is unable to completely determine the actual local configurations, for instance, by Clapp [19], who proposed the probability variation method to obtain the probability distribution of local configurations that maximizes the configurational entropy of alloy. In partic-

ular, multicomponent alloys such as medium-entropy alloys (MEA) and high-entropy alloys are typically associated with enormous configurational space and can thus exhibit complex forms of SRO. For example, our recent theoretical study [20] showed that Si-Ge-Sn MEAs, a promising material for mid-infrared photonics [21–33], carry two distinct forms of SROs. An important implication is that Si-Ge-Sn MEAs can be composed of isocompositional domains with various degrees of SROs, forming a distribution of SROs in real space.

Another type of distribution of SRO is within the order parameter space, which describes the frequency  $f(\alpha_{ij}^m)$  for atoms adopting a specific local atomic SRO configuration  $\alpha_{ij}^m$  which is defined as

$$\alpha_{ij}^m = 1 - \frac{N_{ij}^m}{N_{0,ij}^m}, \quad (2)$$

where  $N_{0,ij}^m$  and  $N_{ij}^m$  are the numbers of  $i$ - $j$  pairs around the reference atom  $i$  in the  $m$ th coordination shell, for a random alloy and the specific configuration, respectively. For example, in diamond cubic lattice, an atom  $i$  can have five possible numbers of  $i$ - $j$  pairs for its first nearest neighbor  $N_{ij}^1$ , ranging from zero to four, corresponding to five possible local atomic SRO parameters  $\alpha_{ij}^1$ .

The average SRO parameter  $\overline{\alpha}_{ij}^m$  is related to  $\alpha_{ij}^m$  through the distribution  $f(\alpha_{ij}^m)$  which describes the occurring frequency of each local atomic SRO parameter:

$$\overline{\alpha}_{ij}^m = \sum f(\alpha_{ij}^m) \alpha_{ij}^m. \quad (3)$$

Clearly, the average SRO parameter  $\overline{\alpha}_{ij}^m$  is incapable of differentiating the distinct distributions that yield the same mean. One schematic example is illustrated in Fig. 1: By definition, a binary random alloy with 50% solute has an average SRO parameter of zero and its distribution exhibits a symmetric bell shape [Fig. 1(a)]. Hypothetically, there can exist other

\*tsli@email.gwu.edu

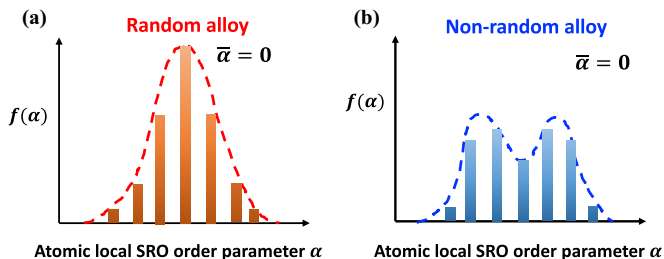


FIG. 1. Schematic diagrams of distributions of SRO parameter  $\alpha$  for (a) a random alloy and (b) a hypothetical nonrandom alloy with 50% solute.  $\bar{\alpha}$  denotes the average of  $\alpha$  and  $f(\alpha)$  denotes the occurring frequency of  $\alpha$ .

distributions, for example, a bimodal distribution of SRO parameter, as shown in Fig. 1(b), that can bear the same aver-

age but actually corresponds to nonrandom alloy structures. Although this is only a hypothetical example, it illustrates the need for accounting for the underlying distribution of SRO parameters to correctly describe alloy's structures. In this work, we show examples in Si-Ge-Sn MEAs where different alloy structures can yield the same average SRO parameters but can only be differentiated through their distributions. We further demonstrate that the distribution of local atomic SRO parameters carries crucial structural features that contribute substantially to the electronic structures of Si-Ge-Sn alloy systems.

Our previous MC/DFT study [20] identifies the spontaneous occurrence of two energy basins, corresponding to two types of SROs in  $\text{Si}_{0.5}\text{Ge}_{0.25}\text{Sn}_{0.25}$ : a regular-SRO (R-SRO) occurring in the high energy basin and an enhanced-SRO (E-SRO) in the low energy basin, both of which are significantly lower in energy than a random alloy [Fig. 2(a)].

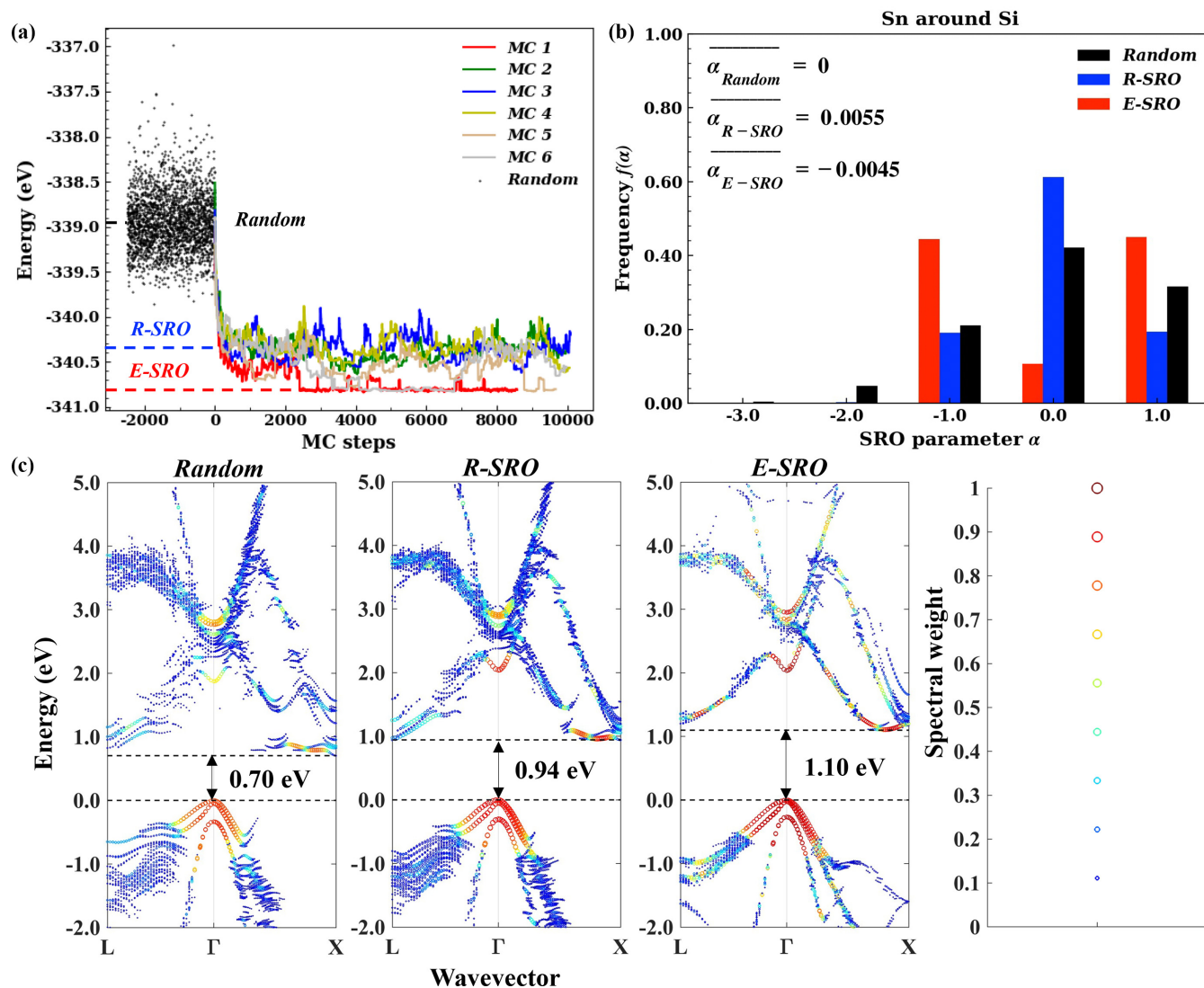


FIG. 2. Distinct structures and properties due to different types of SRO in  $\text{Si}_{0.5}\text{Ge}_{0.25}\text{Sn}_{0.25}$ . (a) The overlay of six independent MC/DFT trajectories and one random sampling identify three energy levels corresponding to three types of ordering: random (black dashed line), R-SRO (blue dashed line), and E-SRO (red dashed line). (b) The distinct distributions of 1NN Si-Sn (Sn around Si) local atomic SRO parameter of random (black), R-SRO (blue), and E-SRO (red) albeit nearly identical average SRO parameters. (c) Calculated electronic band structures for random, R-SRO, and E-SRO in  $\text{Si}_{0.5}\text{Ge}_{0.25}\text{Sn}_{0.25}$  by the spectral weight approach [34,35]. The corresponding Bloch spectral weight is color coded in the legend on the right.

three structures show distinct SRO signatures [20], but intriguingly, nearly identical average first-nearest-neighbor (1NN) Si-Sn SRO parameter  $\overline{\alpha_{\text{SiSn}}^1}$ . As shown by Fig. 2(b), a random solution displays a skewed, discrete bell-shaped distribution  $f(\alpha_{\text{SiSn}}^1)$ . In comparison, the distribution of R-SRO is found to still maintain the bell shape but showing a reduced peak width and enhanced peak height due to SRO. For E-SRO, the distribution becomes a nonbell shape by displaying a valley sandwiched between the two peaks on both sides. These distinctions in the SRO distribution clearly show the significant differences in the arrangement of Si-Sn 1NN among the random, R-SRO, and E-SRO, yet such differences are unable to be differentiated by the average Si-Sn SRO parameter  $\overline{\alpha_{\text{SiSn}}^1}$ . Further calculation shows random, R-SRO, and E-SRO structures carry distinct band structures and the band gap is found to increase with the sequence of random, R-SRO, and E-SRO [Fig. 2(c)]. This suggests the average SRO parameter as the sole metric cannot unravel the key differences in both SRO structure and electronic structure of  $\text{Si}_{0.5}\text{Ge}_{0.25}\text{Sn}_{0.25}$ .

The result naturally prompts the next question as to how much variation in material properties can be attributed to the difference in the distribution of SRO parameters. To address this question, we develop a method to create special structures matching a target structural input, based on the simulated annealing algorithm for structural optimization. As detailed in the Appendix, by setting the objective function to be the average deviation from either the target average SRO parameter  $\overline{\alpha_{ij}^m}$  or the distribution of SRO parameter  $f(\alpha_{ij}^m)$ , we can obtain the corresponding special structures that can represent the key structural feature of the targeted average SRO parameter or the distribution, respectively, by minimization through simulated annealing. The similar idea was previously employed to obtain the special quasirandom structures to represent a random alloy [36,37].

Employing the developed approach, we first examine binary GeSn alloy. Our previous theoretical study predicted a strong SRO in GeSn alloy [38] which was experimentally confirmed through extended x-ray absorption fine structure [39]. At about 25% Sn content, the SRO in GeSn was found to reach the maximum degree, yielding an average 1NN Ge-Sn SRO parameter  $\overline{\alpha_{\text{GeSn}}^1}$  around  $-0.25$ . The calculated local atomic SRO parameter distributions [Figs. 3(a) and 3(b)] provide the details of the deviation from a random alloy. The SRO is subsequently found to yield both a significant decrease in energy [Fig. 3(c)] and a substantial increase in electronic band gap [Fig. 3(d)]. Specifically, a random sampling of  $\text{Ge}_{0.75}\text{Sn}_{0.25}$  leads to an average direct band gap of  $-0.03$  eV, consistent with the previous theoretical prediction based on a random solution model that suggests a transition from negative to positive direct band gap occurs around 25% Sn [40]. In contrast, when taking SRO into account, the ensemble-averaged direct band gap obtained by MC sampling is found to increase to  $0.15$  eV [Fig. 3(d)], yielding a much better agreement with experimental measurement [41]. Employing the developed special structure method, we first generate the optimized structures matching the average 1NN SRO parameters only. As shown in Figs. 3(c) and 3(d), the calculated energies and direct band gaps for these special structures are indeed found to move toward those of SRO configurations obtained by MC

sampling but still exhibit a large difference. This indicates that the average SRO parameters capture some structural information of SRO but are not sufficient to enable reproducing the key properties. In comparison, the generated special structures matching the distributions of SRO parameters are found to further improve the description of both energy [Fig. 3(c)] and direct band gap [Fig. 3(d)], clearly indicating that the distribution of SRO parameters carries important structural information that contributes to the properties of GeSn.

We then consider another interesting material system, binary SiSn alloy, where our recent study also has predicted a significant SRO behavior [42]. Similar to GeSn, the SRO in SiSn alloy leads to a substantial decrease in energy (23 meV/atom) [Fig. 4(c)] and a significant increase in direct band gap (0.4 eV) [Fig. 4(d)], but unlike GeSn, the calculated average 1NN Si-Sn SRO parameter is found to be around  $-0.064$ , which is virtually identical to that (zero) of a random solid solution. Clearly, using the average 1NN SRO parameter as the sole metric, one would barely even discern the existence of SRO in SiSn. Instead, a closer examination of the distributions of 1NN SRO parameters [Figs. 4(a) and 4(b)] clearly shows the distinction between SRO and random configurations. Specifically, the SRO in  $\text{Si}_{0.75}\text{Sn}_{0.25}$  alloy is featured by a significantly higher population of  $\alpha_{\text{SiSn}}^1 = 0$  than that of a random alloy. For a Sn composition of 25%, an  $\alpha_{\text{SiSn}}^1 = 0$  corresponds to the local structural motif with a Si atom having exactly one Sn atom as its nearest neighbor. The enhanced distribution at  $\alpha_{\text{SiSn}}^1 = 0$  means the SRO in  $\text{Si}_{0.75}\text{Sn}_{0.25}$  favors such local Si-Sn arrangement. Interestingly, the preference of this local structural motif is found to be balanced by the decrease in the populations of the other four possible local arrangements of Si-Sn, subsequently yielding an overall Si-Sn first coordination number virtually identical to that of a random alloy. Again this reinforces the conclusion drawn from the aforementioned Si-Ge-Sn MEAs that SRO behavior should be determined based on the underlying distribution rather than its mean. Not surprisingly, the special structures generated by matching the average 1NN SRO parameters lead to energies [Fig. 4(c)] and direct band gaps [Fig. 4(d)] similar to those in random configurations. In contrast, the structures matching the distribution of 1NN SRO parameters are found to improve the description of both properties, showing a decrease in total energy [Fig. 4(c)] and a significant increase in direct band gaps [Fig. 4(d)], moving toward the target properties. We note there still exist sizable differences in both energy and band gap obtained between the special structures matching the 1NN SRO distribution and MC sampling. However, such differences are not unexpected because the structural constraint in the optimization of our study only concerns the first coordination shell. In this regard, our previous study [42] showed the SRO behavior in SiSn alloy is also reflected by the strong ordering occurring in the second coordination shell. The inclusion of these further structural details is expected to continue shrinking the gap between special structures and MC sampling.

In summary, the explicit examples in Si-Ge-Sn, GeSn, and SiSn alloys clearly demonstrate that the average SRO parameter alone is insufficient to fully unveil the structural signature of alloys. These examples show alloys can exhibit identical average SRO parameters while displaying significantly dis-

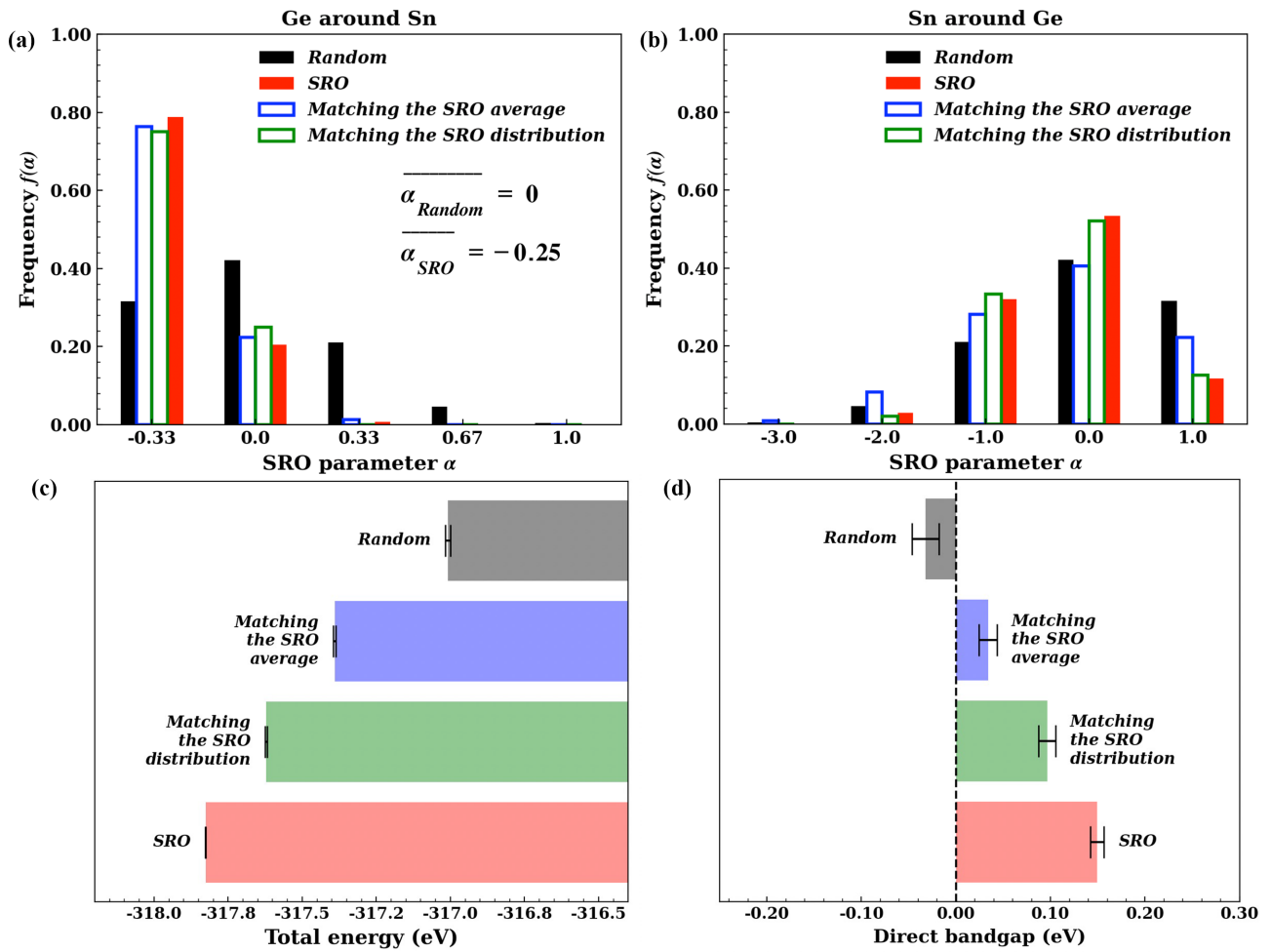


FIG. 3. (a) and (b) show the distributions of INN Ge-Sn SRO parameter for random solid solution (black) solely depending on the composition and SRO configurations (red) obtained through MC sampling in  $\text{Ge}_{0.75}\text{Sn}_{0.25}$ . (c) Total energies and (d) direct band gaps of special structures matching the average (blue) or distributions (green) of INN SRO parameters compared with those of random (black) and SRO (red) configurations in  $\text{Ge}_{0.75}\text{Sn}_{0.25}$ , respectively. The total energies of random and SRO alloys are obtained through random sampling containing  $\sim 1000$  steps and MC/DFT sampling (see the Appendix) consisting of  $\sim 6500$  steps (excluding the first 500 steps for equilibration), respectively. The mean total energies for the generated special structures are averaged over 1000 special structures that match either the average SRO parameter (purple) or the distributions of local atomic SRO parameters (green). The band gaps are obtained by averaging 50 configurations randomly selected from the corresponding ensembles of special structures. The error bars represent the standard errors of the mean.

tinct distributions of local atomic SRO parameters, resulting in remarkable differences in electronic band structures. The finding highlights the role of atomic site distribution in alloys. In fact, for alloy systems, only two types of distributions are rigorously defined: completely ordered and completely random, both of which are bound with strong structural constraints. Being completely ordered is certainly not rare, for example, in compound, but being completely random may not be as common as assumed either, because correlations among alloying elements can easily yield a deviation from the truly random distribution. In this regard, the deviation can manifest itself through two different ways: It can lead to a change in the average local structure, for example, an average coordination number or average SRO parameter distinguished from those of a random alloy. Indeed, such a change has been the key structural signature of SRO to focus on by many studies [9–13,15,16,18]. Alternatively, the

deviation from random can also proceed by forming a distinct distribution of local structures while keeping the average local structure intact. The corresponding SRO structure in this manner may be misinterpreted as random alloy if the average SRO parameter is used as the only structural metric. Although this may seem to be a less common scenario, the identified cases in this study do show its relevance in Si-Ge-Sn alloy systems.

Furthermore, our study underscores the significance of fine structural details in Si-Ge-Sn alloys in the broader context of the general structure-property relationship. Our prior studies [20,38,42] have already demonstrated the nominal alloy composition, which is a coarse-grained structural descriptor, is insufficient to univocally determine alloy’s properties, because the finer-level structural details through SRO can substantially change alloys’ electronic structures. Expanding on this, the current work shows the structural details at an

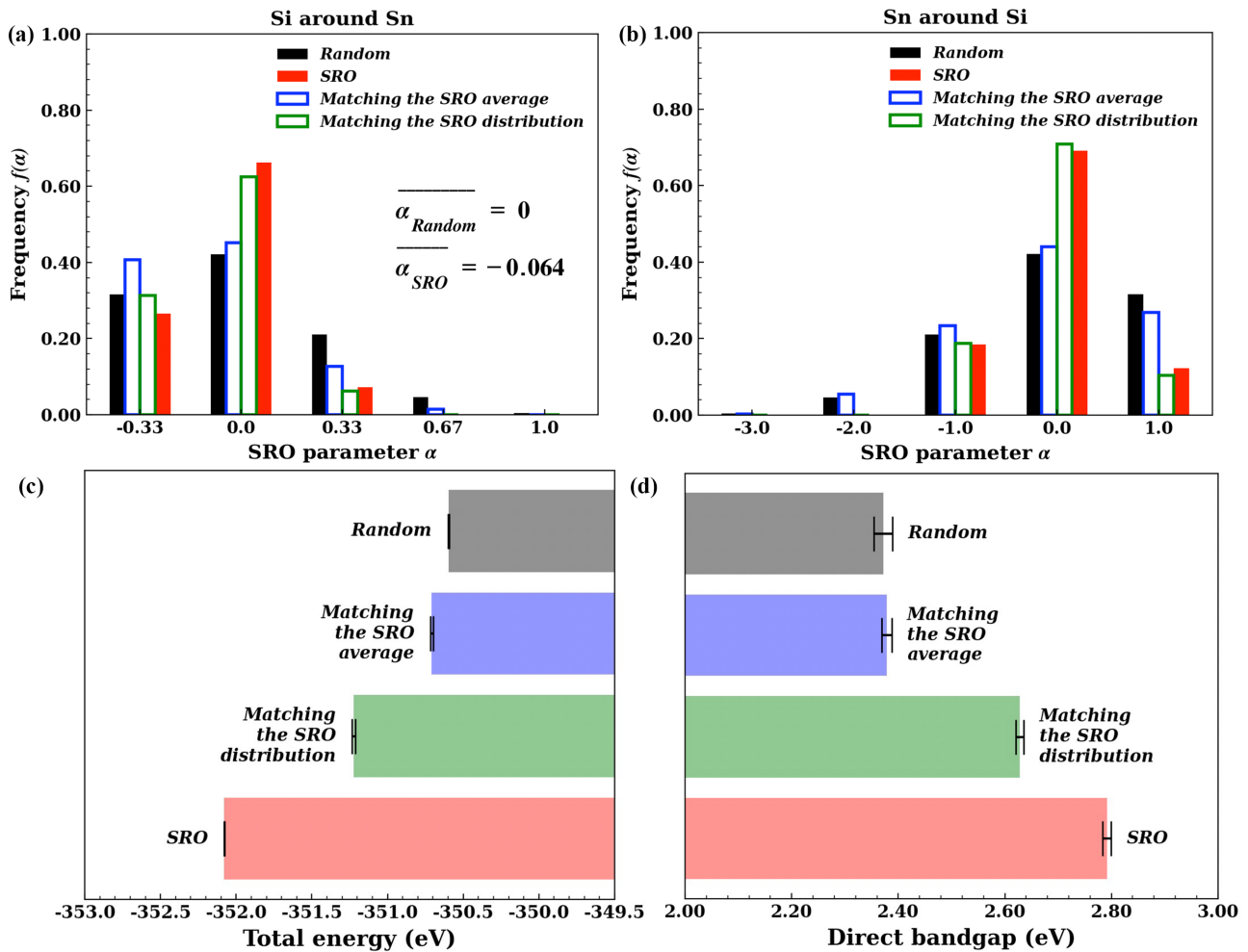


FIG. 4. (a) and (b) show the distributions of 1NN Si-Sn SRO parameter for random solid solution (black) solely depending on the composition and SRO configurations (red) obtained through MC sampling in  $\text{Si}_{0.75}\text{Sn}_{0.25}$ . (c) Total energies and (d) direct band gaps of special structures matching the average (blue) or distributions (green) of 1NN SRO parameters compared with those of random (black) and SRO (red) configurations in  $\text{Si}_{0.75}\text{Sn}_{0.25}$ , respectively. The total energies and direct band gaps are obtained through the same procedure as described for  $\text{Ge}_{0.75}\text{Sn}_{0.25}$  [Figs. 3(c) and 3(d)], except that four independent MC/DFT trajectories each of which contains around 10 000 to 40 000 steps, and random sampling of  $\sim 4500$  steps are used to sample the SRO and random alloys, respectively.

even finer level, as reflected by the distribution of atomic SRO parameter, are also vital for the underlying electronic structures. This highlights the complexity in developing a robust structure-property relationship in these particular alloy systems. It is important to note that while this complexity may not be unboundedly generalized to other alloys or properties, certain types of properties that are sensitive to local atomic structures, e.g., electronic [20,38,42], topological, vibrational [43], and transport [6], may be likely to exhibit similar complexity. We also note that experimental characterization of structural details at such a fine level is challenging, as it requires accurate determination of both chemical environment and position of each atom. In principle, this could be achieved by atom probe tomography (APT) which offers 3D reconstruction of atomic sites in alloy. However, the limited detection efficiency and spatial resolution of APT make it unsuitable to interpret the raw data directly for SRO characterization [44]. In this regard, effort in overcoming the limit of APT through a post-processing reconstruction of structural in-

formation [44] can be a promising approach for characterizing SRO and its distribution.

This work was supported as part of the  $\mu$ -ATOMS, an Energy Frontier Research Center funded by the U.S. Department of Energy, Office of Science, Basic Energy Sciences under Award DE-SC0023412. The authors acknowledge NERSC and GW High Performance Computing for the computing support.

T.L. conceived and supervised the research; X.J., S.C., and T.L. performed the numerical simulations; X.J., C.L., and T.L. analyzed the results; X.J. and S.C. performed the validation. All authors contributed to the writing of the manuscript.

#### Appendix

**1. MC/DFT sampling.** To obtain the ensemble-averaged alloy structures and properties, the Metropolis Monte Carlo (MC) method [45] is employed to sample the configurational space. For each trial move, a new configuration  $j$  is created by randomly selecting and permuting a pair of solute and sol-

vent atoms in configuration  $i$ . The acceptance probability of the new configuration  $j$  is determined by  $\min\{1, \exp(-(E_j - E_i)/k_B T)\}$ , where  $E_i$  and  $E_j$  are the total energies of configuration  $i$  and  $j$ , respectively,  $k_B$  is the Boltzmann constant, and  $T$  is temperature (300 K in this study). The new configuration  $j$  then undergoes a full relaxation to obtain its energy  $E_j$ .

The total energy calculation is based on density functional theory (DFT) implemented in Vienna *ab initio* simulation package (VASP) [46] based on the projector augmented wave method [47–49]. Local density approximation (LDA) [50] is employed for the exchange-correlation functional, which has been shown to yield the best agreement with experiments on pure Ge and Sn for geometry optimization [40,51–53]. A simulation cell containing 64 atoms is obtained by replicating a conventional diamond cubic (DC) cell including eight atoms twice along each dimension. Our previous investigations have shown this system size is sufficient to describe the SRO structures in Si-Ge-Sn alloy systems [20,38]. A  $2 \times 2 \times 2$  Monkhorst-Pack  $k$ -points grid [54] and a plane-wave cutoff energy of 300 eV are applied for structural relaxation (including cell volume, cell shape, and atomic positions) for each MC step, combined with the convergence criteria of  $10^{-4}$  eV and  $10^{-3}$  eV for electronic and ionic relaxations, respectively.

2. *Simulated annealing.* The simulated annealing algorithm is adopted to optimize structures based on SRO parameters, thus the optimization process is essentially equivalent to generating special quasirandom structures (SQS) [36,37], except that here the objective functions are defined to target at SRO parameters.

To optimize the structures based on the average SRO parameters, the objective function  $Q$  computes the average deviation (in percentage) to the targeted average SRO parameters obtained through MC/DFT sampling, which is defined as

$$Q = \frac{1}{N_{\text{pairs}} N_{\text{shells}}} \sum_{i=1}^{N_{\text{shells}}} \sum_{j=1}^{N_{\text{pairs}}} \left| \frac{\Delta \alpha_{ij}}{\alpha_{ij}^{\text{target}}} \right| \times 100\%, \quad (\text{A1})$$

where  $N_{\text{pairs}}$  is the total number of independent pairs, for instance,  $N_{\text{pairs}} = 1$  for a binary alloy,  $N_{\text{pairs}} = 3$  for a ternary alloy.  $N_{\text{shells}}$  is the total number of shells considered, for instance,  $N_{\text{shells}} = 1$  considers the first shell, and  $N_{\text{shells}} = 2$  considers both the first and second shells.  $\Delta \alpha_{ij}$  computes the deviation in average SRO parameter  $\alpha_{ij}$  from the targeted average SRO parameter  $\alpha_{ij}^{\text{target}}$ .

To optimize the structures based on the distributions of SRO parameters, the objective function  $Q$  computes the total deviation to the targeted distributions obtained through MC/DFT sampling, which is defined as

$$Q = \sum_{i=1}^{N_{\text{shells}}} \sum_{j=1}^{N_{\text{pairs}}} \sum_{k=1}^M |\Delta \gamma_{ijk}|, \quad (\text{A2})$$

where  $M$  is the total number of possible values of SRO parameters, which equals to 1 + the total number of nearest neighbors at a given shell. Since diamond cubic structure has four total first-nearest neighbors and twelve second-nearest neighbors,  $M = 5$  for the first shell, and  $M = 13$  for the second shell.  $|\Delta \gamma_{ijk}|$  measures the deviation in the occurring frequency for a specific local SRO parameter  $k$  at the shell  $i$  for pair  $j$ . Thus,  $Q$  is the total deviation with respect to the targeted distribution.

The objective function is then adopted by a simulated annealing process based on the Metropolis algorithm [45], with the acceptance probability for a new configuration  $j$  generated from a trial move in configuration  $i$  being  $\min\{1, \exp(-(Q_j - Q_i)/T)\}$ .  $T$  is a user-specified fictitious temperature which is used to control the convergence of simulated annealing. Generally, a lower  $T$  can enhance the speed of structural optimization toward the target, while a higher  $T$  can be beneficial in preventing the optimization process from getting stuck in a local minimum. Based on the definition of the objective function  $Q$ , when  $Q = 0$ , the structures are fully optimized with either its average SRO or the distributions of local atomic SRO parameters identical to the target.

3. *Band structure calculations.* The modified Becke-Johnson (mBJ) exchange potential [53] is employed for band structure calculations performed in VASP code, which has been demonstrated to compute the correct bandgaps of Si, Ge, and  $\alpha$  Sn with the  $c$ -mBJ parameter set to be 1.2 and with a substantial reduction in computational cost with respect to the hybrid functionals or GW methods [40,51,53]. The spectral weight approach is used [34,35] to unfold the band structures computed based on 64-atom cell back into the first Brillouin Zone of diamond cubic structure using the code *fold2bloch* [35]. Relativistic effects (spin-orbit coupling) are included in the band structure calculation, which has been demonstrated to be crucial for reproducing the band structures of Ge and  $\alpha$  Sn [40,51].

- 
- [1] R. Zhang, S. Zhao, C. Ophus, Y. Deng, S. J. Vachhani, B. Ozdol, R. Traylor, K. C. Bustillo, J. Morris Jr., D. C. Chrzan *et al.*, Direct imaging of short-range order and its impact on deformation in Ti-6Al, *Sci. Adv.* **5**, eaax2799 (2019).
- [2] R. Zhang, S. Zhao, J. Ding, Y. Chong, T. Jia, C. Ophus, M. Asta, R. O. Ritchie, and A. M. Minor, Short-range order and its impact on the CrCoNi medium-entropy alloy, *Nature (London)* **581**, 283 (2020).
- [3] Y. Wu, F. Zhang, X. Yuan, H. Huang, X. Wen, Y. Wang, M. Zhang, H. Wu, X. Liu, H. Wang, S. Jiang, and Z. Lu, Short-range ordering and its effects on mechanical properties of high-entropy alloys, *J. Mater. Sci. Technol.* **62**, 214 (2021).
- [4] B. Jiang, Y. Yu, J. Cui, X. Liu, L. Xie, J. Liao, Q. Zhang, Y. Huang, S. Ning, B. Jia, B. Zhu, S. Bai, L. Chen, S. J. Pennycook, and J. He, High-entropy-stabilized chalcogenides with high thermoelectric performance, *Science* **371**, 830 (2021).
- [5] S. Roychowdhury, T. Ghosh, R. Arora, M. Samanta, L. Xie, N. K. Singh, A. Soni, J. He, U. V. Waghmare, and K. Biswas, Enhanced atomic ordering leads to high thermoelectric performance in AgSbTe<sub>2</sub>, *Science* **371**, 722 (2021).
- [6] H. Ji, A. Urban, D. A. Kitchaev, D.-H. Kwon, N. Artrith, C. Ophus, W. Huang, Z. Cai, T. Shi, J. C. Kim, H. Kim, and G. Ceder, Hidden structural and chemical order controls lithium

- transport in cation-disordered oxides for rechargeable batteries, *Nat. Commun.* **10**, 592 (2019).
- [7] F. X. Zhang, S. Zhao, K. Jin, H. Xue, G. Velisa, H. Bei, R. Huang, J. Y. P. Ko, D. C. Pagan, J. C. Neufeind, W. J. Weber, and Y. Zhang, Local structure and short-range order in a NiCoCr solid solution alloy, *Phys. Rev. Lett.* **118**, 205501 (2017).
- [8] X. Chen, Q. Wang, Z. Cheng, M. Zhu, H. Zhou, P. Jiang, L. Zhou, Q. Xue, F. Yuan, J. Zhu *et al.*, Direct observation of chemical short-range order in a medium-entropy alloy, *Nature (London)* **592**, 712 (2021).
- [9] S. Yin, J. Ding, M. Asta, and R. O. Ritchie, Ab initio modeling of the energy landscape for screw dislocations in body-centered cubic high-entropy alloys, *npj Comput. Mater.* **6**, 110 (2020).
- [10] S. Yin, Y. Zuo, A. Abu-Odeh, H. Zheng, X.-G. Li, J. Ding, S. P. Ong, M. Asta, and R. O. Ritchie, Atomistic simulations of dislocation mobility in refractory high-entropy alloys and the effect of chemical short-range order, *Nat. Commun.* **12**, 4873 (2021).
- [11] F. Walsh, M. Asta, and R. O. Ritchie, Magnetically driven short-range order can explain anomalous measurements in CrCoNi, *Proc. Natl. Acad. Sci.* **118**, e2020540118 (2021).
- [12] J. Ding, Q. Yu, M. Asta, and R. O. Ritchie, Tunable stacking fault energies by tailoring local chemical order in CrCoNi medium-entropy alloys, *Proc. Natl. Acad. Sci.* **115**, 8919 (2018).
- [13] T. Kostiuhenko, A. V. Ruban, J. Neugebauer, A. Shapeev, and F. Körmann, Short-range order in face-centered cubic VCoNi alloys, *Phys. Rev. Mater.* **4**, 113802 (2020).
- [14] D. Liu, Q. Wang, J. Wang, X. Chen, P. Jiang, F. Yuan, Z. Cheng, E. Ma, and X. Wu, Chemical short-range order in Fe<sub>50</sub>Mn<sub>30</sub>Co<sub>10</sub>Cr<sub>10</sub> high-entropy alloy, *Mater. Today Nano* **16**, 100139 (2021).
- [15] X. Huang, L. Liu, X. Duan, W. Liao, J. Huang, H. Sun, and C. Yu, Atomistic simulation of chemical short-range order in HfNbTaZr high entropy alloy based on a newly-developed interatomic potential, *Mater. Des.* **202**, 109560 (2021).
- [16] S. D. Wang, X. J. Liu, Z. F. Lei, D. Y. Lin, F. G. Bian, C. M. Yang, M. Y. Jiao, Q. Du, H. Wang, Y. Wu, S. H. Jiang, and Z. P. Lu, Chemical short-range ordering and its strengthening effect in refractory high-entropy alloys, *Phys. Rev. B* **103**, 104107 (2021).
- [17] J. M. Cowley, An approximate theory of order in alloys, *Phys. Rev.* **77**, 669 (1950).
- [18] A. Tamm, A. Aabloo, M. Klintonberg, M. Stocks, and A. Caro, Atomic-scale properties of Ni-based fcc ternary, and quaternary alloys, *Acta Mater.* **99**, 307 (2015).
- [19] P. C. Clapp, Atomic configurations in binary alloys, *Phys. Rev. B* **4**, 255 (1971).
- [20] X. Jin, S. Chen, and T. Li, Coexistence of two types of short-range order in Si-Ge-Sn medium-entropy alloys, *Commun. Mater.* **3**, 66 (2022).
- [21] R. A. Soref and C. H. Perry, Predicted band gap of the new semiconductor SiGeSn, *J. Appl. Phys.* **69**, 539 (1991).
- [22] F. Gencarelli, B. Vincent, J. Demeulemeester, A. Vantomme, A. Moussa, A. Franquet, A. Kumar, H. Bender, J. Meersschaat, W. Vandervorst, R. Loo, M. Caymax, K. Temst, and M. Heyns, Crystalline properties and strain relaxation mechanism of CVD grown GeSn, *ECS J. Solid State Sci. Technol.* **2**, P134 (2013).
- [23] S. Wirths, D. Buca, and S. Mantl, Si-Ge-Sn alloys: From growth to applications, *Prog. Cryst. Growth Charact. Mater.* **62**, 1 (2016).
- [24] S. A. Ghetmiri, W. Du, J. Margetis, A. Mosleh, L. Cousar, B. R. Conley, L. Domulevicz, A. Nazzal, G. Sun, R. A. Soref, J. Tolle, B. Li, H. A. Naseem, and S.-Q. Yu, Direct-bandgap GeSn grown on silicon with 2230 nm photoluminescence, *Appl. Phys. Lett.* **105**, 151109 (2014).
- [25] S. Wirths, R. Geiger, N. von den Driesch, G. Mussler, T. Stoica, S. Mantl, Z. Ikonic, M. Luysberg, S. Chiussi, J. M. Hartmann, H. Sigg, J. Faist, D. Buca, and D. Grützmacher, Lasing in direct-bandgap GeSn alloy grown on Si, *Nat. Photonics* **9**, 88 (2015).
- [26] D. Stange, S. Wirths, R. Geiger, C. Schulte-Braucks, B. Marzban, N. von den Driesch, G. Mussler, T. Zabel, T. Stoica, J.-M. Hartmann, S. Mantl, Z. Ikonic, D. Grützmacher, H. Sigg, J. Witzens, and D. Buca, Optically pumped GeSn microdisk lasers on Si, *ACS Photonics* **3**, 1279 (2016).
- [27] V. Reboud, A. Gassenq, N. Pauc, J. Aubin, L. Milord, Q. M. Thai, M. Bertrand, K. Guillois, D. Rouchon, J. Rothman, T. Zabel, F. Armand Pilon, H. Sigg, A. Chelnokov, J. M. Hartmann, and V. Calvo, Optically pumped GeSn micro-disks with 16% Sn lasing at 3.1  $\mu\text{m}$  up to 180 K, *Appl. Phys. Lett.* **111**, 092101 (2017).
- [28] S. Al-Kabi, S. A. Ghetmiri, J. Margetis, T. Pham, Y. Zhou, W. Dou, B. Collier, R. Quinde, W. Du, A. Mosleh, J. Liu, G. Sun, R. A. Soref, J. Tolle, B. Li, M. Mortazavi, H. A. Naseem, and S.-Q. Yu, An optically pumped 2.5  $\mu\text{m}$  GeSn laser on Si operating at 110 K, *Appl. Phys. Lett.* **109**, 171105 (2016).
- [29] J. Margetis, S. Al-Kabi, W. Du, W. Dou, Y. Zhou, T. Pham, P. Grant, S. Ghetmiri, A. Mosleh, B. Li, J. Liu, G. Sun, R. Soref, J. Tolle, M. Mortazavi, and S.-Q. Yu, Si-based GeSn lasers with wavelength coverage of 2–3  $\mu\text{m}$  and operating temperatures up to 180 K, *ACS Photonics* **5**, 827 (2018).
- [30] W. Dou, Y. Zhou, J. Margetis, S. A. Ghetmiri, S. Al-Kabi, W. Du, J. Liu, G. Sun, R. A. Soref, J. Tolle, B. Li, M. Mortazavi, and S.-Q. Yu, Optically pumped lasing at 3  $\mu\text{m}$  from compositionally graded GeSn with tin up to 22.3%, *Opt. Lett.* **43**, 4558 (2018).
- [31] M. Kurosawa, M. Kato, T. Yamaha, N. Taoka, O. Nakatsuka, and S. Zaima, Near-infrared light absorption by polycrystalline SiSn alloys grown on insulating layers, *Appl. Phys. Lett.* **106**, 171908 (2015).
- [32] J. Tolle, A. V. G. Chizmeshya, Y. Y. Fang, J. Kouvetakis, V. R. D'Costa, C. W. Hu, J. Menéndez, and I. S. T. Tsong, Low temperature chemical vapor deposition of Si-based compounds via SiH<sub>3</sub>SiH<sub>2</sub>SiH<sub>3</sub>: Metastable SiSn/GeSn/Si(100) heteroepitaxial structures, *Appl. Phys. Lett.* **89**, 231924 (2006).
- [33] T. T. McCarthy, Z. Ju, S. Schaefer, S.-Q. Yu, and Y.-H. Zhang, Momentum (k)-space carrier separation using SiGeSn alloys for photodetector applications, *J. Appl. Phys.* **130**, 223102 (2021).
- [34] V. Popescu and A. Zunger, Effective band structure of random alloys, *Phys. Rev. Lett.* **104**, 236403 (2010).
- [35] O. Rubel, A. Bokhanchuk, S. J. Ahmed, and E. Assmann, Unfolding the band structure of disordered solids: From bound states to high-mobility Kane fermions, *Phys. Rev. B* **90**, 115202 (2014).
- [36] A. van de Walle, P. Tiwary, M. De Jong, D. Olmsted, M. Asta, A. Dick, D. Shin, Y. Wang, L.-Q. Chen, and Z.-K. Liu, Efficient stochastic generation of special quasirandom structures, *Calphad* **42**, 13 (2013).

- [37] A. van de Walle, M. Asta, and G. Ceder, The alloy theoretic automated toolkit: A user guide, *Calphad* **26**, 539 (2002).
- [38] B. Cao, S. Chen, X. Jin, J. Liu, and T. Li, Short-range order in GeSn alloy, *ACS Appl. Mater. Interfaces* **12**, 57245 (2020).
- [39] J. Z. Lentz, J. C. Woicik, M. Bergschneider, R. Davis, A. Mehta, K. Cho, and P. C. McIntyre, Local ordering in Ge/Ge-Sn semiconductor alloy core/shell nanowires revealed by extended x-ray absorption fine structure (EXAFS), *Appl. Phys. Lett.* **122**, 062103 (2023).
- [40] M. Polak, P. Scharoch, and R. Kudrawiec, The electronic band structure of  $\text{Ge}_{1-x}\text{Sn}_x$  in the full composition range: indirect, direct, and inverted gaps regimes, band offsets, and the burstein–moss effect, *J. Phys. D* **50**, 195103 (2017).
- [41] C. Xu, P. M. Wallace, D. A. Ringwala, S. L. Chang, C. D. Poweleit, J. Kouvetakis, and J. Menéndez, Mid-infrared (3–8  $\mu\text{m}$ )  $\text{Ge}_{1-y}\text{Sn}_y$  alloys ( $0.15 < y < 0.30$ ): Synthesis, structural, and optical properties, *Appl. Phys. Lett.* **114**, 212104 (2019).
- [42] X. Jin, S. Chen, and T. Li, Short-range order in SiSn alloy enriched by second-nearest-neighbor repulsion, *Phys. Rev. Mater.* **5**, 104606 (2021).
- [43] A. A. Corley-Wiciak, S. Chen, O. Concepción, M. H. Zoellner, D. Grützmacher, D. Buca, T. Li, G. Capellini, and D. Spirito, Local alloy order in a  $\text{Ge}_{1-x}\text{Sn}_x/\text{Ge}$  epitaxial layer, *Phys. Rev. Appl.* **20**, 024021 (2023).
- [44] S. Liu, A. C. Covian, X. Wang, C. T. Cline, A. Akey, W. Dong, S. Yu, and J. Liu, 3D nanoscale mapping of short-range order in GeSn alloys, *Small Methods*, **6** 2200029 (2022).
- [45] N. Metropolis, A. W. Rosenbluth, M. N. Rosenbluth, A. H. Teller, and E. Teller, Equation of state calculations by fast computing machines, *J. Chem. Phys.* **21**, 1087 (1953).
- [46] G. Kresse and J. Hafner, Ab initio molecular dynamics for liquid metals, *Phys. Rev. B* **47**, 558 (1993).
- [47] G. Kresse and D. Joubert, From ultrasoft pseudopotentials to the projector augmented-wave method, *Phys. Rev. B* **59**, 1758 (1999).
- [48] G. Kresse and J. Furthmüller, Efficiency of ab-initio total energy calculations for metals and semiconductors using a plane-wave basis set, *Comput. Mater. Sci.* **6**, 15 (1996).
- [49] G. Kresse and J. Furthmüller, Efficient iterative schemes for ab initio total-energy calculations using a plane-wave basis set, *Phys. Rev. B* **54**, 11169 (1996).
- [50] D. M. Ceperley and B. J. Alder, Ground state of the electron gas by a stochastic method, *Phys. Rev. Lett.* **45**, 566 (1980).
- [51] C. Eckhardt, K. Hummer, and G. Kresse, Indirect-to-direct gap transition in strained and unstrained  $\text{Sn}_x\text{Ge}_{1-x}$  alloys, *Phys. Rev. B* **89**, 165201 (2014).
- [52] P. Haas, F. Tran, and P. Blaha, Calculation of the lattice constant of solids with semilocal functionals, *Phys. Rev. B* **79**, 085104 (2009).
- [53] F. Tran and P. Blaha, Accurate band gaps of semiconductors and insulators with a semilocal exchange-correlation potential, *Phys. Rev. Lett.* **102**, 226401 (2009).
- [54] H. J. Monkhorst and J. D. Pack, Special points for Brillouin-zone integrations, *Phys. Rev. B* **13**, 5188 (1976).